Korean J. Chem. Eng., 39(2), 440-450 (2022)
DOI: 10.1007/s11814-021-0996-9

pISSN: 0256-1115
eISSN: 1975-7220

Hydrothermal synthesis and characterization of quartz nanocrystals - Implications from a simple kinetic growth model

Gyuseop Moon‡, Eun-Hye Jang‡, Seok Kim, Youngson Choe, and Sungwook Chung†

School of Chemical Engineering, Pusan National University, 2 Busandaehak-ro 63beon-gil, Geumjeong-gu, Busan 46241, Korea

(*Received 20 July 2021 • Revised 13 October 2021 • Accepted 24 October 2021*)

Abstract−Obtaining quartz nanocrystals (NCs) of high purity and uniform sizes remains a challenging problem. In this report, the synthesis and characterization of quartz NCs under hydrothermal conditions was investigated and the corresponding mathematical models were introduced to elucidate the growth kinetics of quartz NCs. Amorphous silica nanoparticles were dissolved in aqueous solutions followed by mild hydrothermal reactions, resulting in NCs with relatively uniform sizes and shapes. The NCs were made from highly crystalline α-quartz. Their hydrothermal growth process over an induction period of ~3 hr initially yielded amorphous silica nanoparticles that were aggregated into clusters. The crystallinity of α-quartz emerged from the products of the nanoparticle clusters after the induction period, which likely involved an amorphous to crystalline transition. The NCs continued to grow with increasing time. The growth kinetics exhibited a dependence on the square root of time, which has not been observed for other quartz nanocrystalline systems. The analysis suggests that the process is reaction-limited, not diffusion-limited, likely governed by the dissolved silicate monomer flux to the surface of the growing NCs followed by first-order rate-limiting attachment kinetics. This study highlights the growth kinetics of quartz NCs by unveiling the complex nature of multi-step growth processes, offering an improved hydrothermal method for fine-tuning the size and morphology of quartz NCs, which have potential optoelectronics, sensing, and rechargeable battery, and novel biorefinery process applications.

Keywords: Quartz, Nanocrystals, Hydrothermal, Growth Kinetics, Reaction-limited Control

INTRODUCTION

Many synthetic techniques, such as microemulsion, sol-gel, in-situ casting, and hydrothermal methods, have been developed to produce novel nanostructures exhibiting large surface area, excellent stability, and unique material properties [1-4]. Silica is one of their main constituents of the functional nanostructures [5-8] that also has a range of uses to make products for improving the quality of life [9]. Crystalline silica exists in at least eight different crystal polymorphs, of which quartz is the abundant form because it is the most thermodynamically stable phase under ambient conditions. Quartz is a chemically inert and relatively hard crystalline mineral that is present in rocks, soil, and sand [10]. It is used widely in many large-scale applications, such as abrasives, foundry materials, ceramics, and cements, because of its abundance and high thermal and chemical stability [11]. Quartz is also used as an active optoelectronic component such as a crystal oscillator for many modern electronic devices, including watches, clocks, radios, personal computers, and cellphones, because of its unique piezoelectric properties [12,13].

Quartz has two polymorphs of α- and β-quartz, which exhibit slightly different helical arrangements of the tetrahedral silicate unit with the ridgepole of one tetrahedron connected to the keel of the next tetrahedron in a helical conformation [14]. β-Quartz has hexagonal symmetry with six- and three-fold screw axes, while the same symmetry elements of α-quartz are distorted slightly to a certain extent. In general, the α-phase is stable at ambient temperature and atmospheric pressure. On the other hand, the β-phase is stable only at temperatures above ~573 °C, and transforms spontaneously to α-quartz upon cooling [15].

The hydrothermal growth of crystals has been studied widely for many years [16-21]. In general, hydrothermal processes employ an autoclave as a reaction apparatus for heating reaction solvents near their critical point simultaneously with autogenous pressure, allowing them to grow highly crystalline materials in large quantities at relatively low cost [21]. Their advantages over other crystal growth processes include creating distinct crystalline phases that may not be thermodynamically stable at the melting point and growing materials with a high vapor pressure near the melting points [22]. Hydrothermal methods are also effective in not only producing bulk quartz [16,17,23-25] from saturated silica solution but also synthesizing isotropic and anisotropic quartz nanocrystals (NCs) [23,26-30] with sizes ranging from tens of nanometers to hundreds of micrometers. Despite the progress, some of the reported synthetic methods did not always have superb control over well-defined sizes, shapes, and crystal phases because of the extremely rapid growth and coarsening processes typically under highly basic (pH>10) hydrothermal conditions [26,28,31]. Although there have been studies on the growth of quartz previously, most of them aimed at growing bulk quartz at high temperature (≥~500 °C) and pressure (≥~100 MPa), because these conditions, which may be reminis-

†To whom correspondence should be addressed.
E-mail: sungwook.chung@pusan.ac.kr
‡These authors contributed equally to this work.

cent of harsh geological environments, are required to increase the solubility of a sparingly soluble material to a point where it can be readily nucleated and crystallized [32,33]. However, few studies have focused on investigating and understanding the nucleation and growth of quartz NCs under relatively moderate hydrothermal [34] and ambient [27] conditions.

Previously, we reported a hydrothermal method to synthesize highly crystalline quartz NCs from the dissolution of amorphous silica nanoparticles (ASNs) in a brief communication [29]. Here, we present a full investigation of the synthesis and characterization of quartz NCs. Also, we intend to follow the growth process of quartz NCs at ~250 °C under autonomous pressure, determine a rate law that may be extrapolated, at least semi-quantitatively, and interpret the growth kinetics by harnessing the theoretical models developed for other nanocrystal growth processes. The hydrothermal reactions of dissolved ASNs in aqueous solutions initially yielded powdery amorphous products of silica nanoparticles over a reaction time of 0-3 hr. The crystallinity of α-quartz emerged from the products after ~3-6 hr, which suggests they likely transformed from amorphous to crystalline silica in solutions. Since the transition, the growth of quartz NCs proceeded continuously until almost all the precursors were consumed. Analyses of the growth kinetics over the time period of 0-24 hr revealed a dependence on the square root of time, leading to a simple kinetic model in which the growth process that is likely governed by the monomeric dissolved silicate precursor flux to the surface of growing NCs followed by first-order rate-limiting attachment kinetics, which provides a rationale for the reaction-limited growth process.

EXPERIMENTAL SECTION

1. Materials

Tetraethyl orthosilicate (TEOS, ≥99%) was purchased from Sigma-Aldrich (USA) and used as received. All other chemicals including methanol, absolute ethanol, acetone, ammonium hydroxide aqueous solution (NH_4OH, 25 wt%, Daejung, Korea), 1 N sodium hydroxide (NaOH, Samchun, Korea), and 1 N hydrochloric acid (HCl, Samchun, Korea) were of analytical ACS Regent grade and used as received.

2. Preparation of Quartz NCs

Quartz NCs were synthesized via hydrothermal methods previously reported elsewhere [29]. An aqueous solution of 0.225 g amorphous silica nanoparticles (ASNs) prepared using a slightly modified Stöber process [6] mixed with 27 mL triply distilled H_2O and 3 mL 1 N NaOH solution was heated to 100 °C and stirred at 400 rpm for 1 hr. The solution turned from opaque white to clear after ~20 min, due likely to the complete dissolution of ASNs at pH≥~12. After 1 hr, ~1 mL of 1 N HCl was added to eliminate the excess hydroxyl ions by adjusting the pH of the solution to ~7.0. The resulting aqueous solution was transferred to a 50 mL polyetheretherketone (PEEK)-lined stainless steel autoclave and heated to ~250 °C for 3-24 hr. Once the reaction was complete, the autoclave was cooled slowly to room temperature. The white precipitates were then filtered through a nylon membrane with a pore diameter of 0.25 μm, washed with an excess of deionized water and anhydrous ethanol and dried in a vacuum oven at room temperature to give ~120 mg of the NCs.

3. Characterization

X-ray powder diffraction (XRD, X'Pert-MPD, Philips Inc., USA) of the NCs was conducted using a monochromatized source of Cu Kα_1 radiation (λ=0.15405 nm) at 1.2 kW power (40 kV, 30 mA). Fourier transform infrared spectroscopy (FT-IR, Spectrum GX, Perkin Elmer Inc., USA) was performed using the KBr pellet and attenuated total reflection (ATR) techniques. X-ray photoelectron spectroscopy (XPS, ESCALAB 250, Thermo Fisher Scientific Inc., USA) of the NCs was performed using a monochromatic X-ray source of an Al anode Kα radiation (1,486.6 eV) as an excitation source. The binding energy was calibrated to the C 1s line of carbon at 284.6 eV before the actual measurements. Thermal analyses of the NCs involved using thermal gravimetric analysis (TGA, Q50, Waters™ & TA Instruments, USA) analyzer. Typically ~15 mg of the synthesized NCs was heated in an Al_2O_3 crucible at a heating rate of 5 °C/min under N_2 flow of 100 mL/min up to 800 °C. N_2 adsorption-desorption measurements of the NCs were performed using Autopore IV and ASAP 2010 instrument (Micromeritics Instrument Corporation, USA). Samples of the NCs were degassed at 300 °C for ~3 h before the measurements. The Brunauer-Emmett-Teller (BET) method was used to calculate the specific surface areas. ^{29}Si solid-state nuclear magnetic resonance (ssNMR) spectroscopy of the NCs and ASNs was performed on a 400 MHz AVANCE III HD NMR spectrometer (Bruker Corporation) equipped with a 4 mm (outer diameter of the zirconia rotor) magic angle spinning (MAS) probe at the Korea Basic Science Institute (KBSI, Western Seoul Center, Korea). The spectra were obtained by direct excitation at 79.51 MHz with a 1.6 μs pulse width (pulse angle π/6), a 50 s recycle delay at ambient probe temperature (~25 °C), and a sample spin rate of 11 kHz. The signals from 4900 scans were accumulated. The ^{29}Si ssNMR chemical shifts (δ in ppm) were referenced to an external sample of tetrakis(trimethylsilyl) silane at −135.5 ppm with respect to tetramethylsilane (TMS) at 0.0 ppm. The morphology of the NCs was examined by field emission scanning electron microscopy (FESEM, Zeiss Supra 25, Zeiss International, Germany) with an accelerating voltage ranging from 5 to 10 kV. Transmission electron microscopy (TEM, H-7600, Hitachi High-tech, Germany) of the NCs was performed at an accelerating voltage of 80 kV. The size and shape characterization of NCs was based on FESEM and TEM image analysis. As long as the NCs are approximately spherical (i.e., isotropic), the only relevant length scale is the diameter of NC. However, when they become non-spherical, their structural anisotropy requires two parameters, such as length and width, for complete size and shape characterization. Therefore, the former was determined by measuring the maximum sizes from TEM images of individual NCs. Then, the latter was determined by measuring the sizes perpendicular to the long axis for the length. Fiji, a distribution of open-source ImageJ software, was used to analyze all images to obtain the mean values of length and width and the corresponding error bars representing the standard deviations (based on ≥~50 counts/image). High-resolution TEM (HRTEM) and selected area electron diffraction (SAED) were performed on a TALOS F200X TEM (FEI & Thermo Fisher Scientific Electron Microscopy Solutions, USA) at an acceleration voltage of 200 kV. Lattice spacing and angle mea-

surements were taken from Fourier analysis of individual NC's HRTEM images that were properly tilted down a specific low order zone [35,36]. The idealized crystal habits of α-quartz were modeled using stereographic projections by the Visualization of Electronic and STructural Analysis (VESTA) and KrystalShaper® (JCrystalSoft) software packages.

RESULTS AND DISCUSSION

Fig. 1 is a schematic diagram of preparing quartz NCs via hydrothermal methods. Fig. 2 shows the structural analysis of quartz NCs by XRD, FESEM, and HRTEM. The powder XRD patterns of the as-synthesized NCs indicated their crystalline nature (blue curve, Fig. 2A). The majority of peaks in the XRD pattern were in accordance with that of bulk α-quartz (red curve, Fig. 2A, Joint Committee on Powder Diffraction Standards (JCPDS) card no. 46-1045). FESEM image revealed that the NCs had a prism-like morphology [37] with two six-sided pyramids at both ends. Based on FESEM measurements (Fig. S2), the average size of the NCs synthesized from ~6 hr reaction time was measured to be 407±16 nm. HRTEM of a typical NC revealed lattice fringes with a lattice spacing of 0.33 and 0.43 nm, which corresponded to the (101) and (100) crystallographic planes of α-quartz, respectively (Fig. 2C) [38,39]. The interfacial angle between the (100) and (101) planes was ~38.1°, which was reasonably consistent with the value of ~38.2° from the model of bulk α-quartz crystal shown in the inset image of Fig. 2B [38, 39]. The selected area electron diffraction (SAED) pattern of typical quartz NCs (Fig. S1) and the Fast Fourier transform (FFT) of

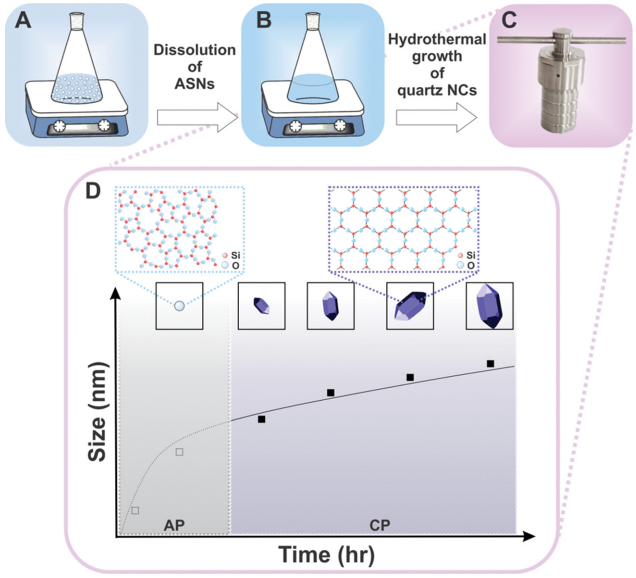

Fig. 1. Schematic diagram of the hydrothermal synthesis of quartz nanocrystals (NCs). (A) Use of amorphous silica nanoparticles (ASNs) as starting materials. (B) Complete dissolution of ASNs in aqueous solutions. (C) Hydrothermal reaction at ~250 °C under an autogenic pressure. (D) Growth kinetics of α-quartz NCs via amorphous phase (AP) to crystalline phase (CP) transition.

HRTEM image (Fig. 2D) show an ordered pattern of diffraction spots assigned to the {100} and {101} planes based on the *d*-spac-

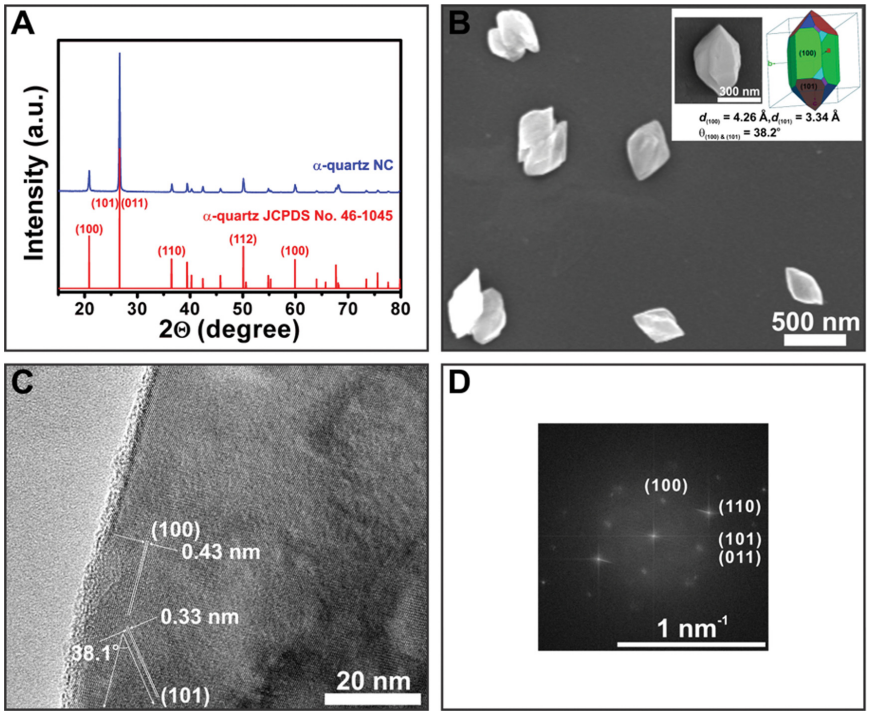

Fig. 2. (A) XRD patterns of α-quartz NCs (blue curve). (B) Higher magnification FESEM image of α-quartz NCs and inset image showing the comparison of the prism-like morphology of single α-quartz NC (left) and a computer-generated 3D model of bulk α-quartz crystal with (100) and (101) crystallographic planes (right). (C) Representative HRTEM image of α-quartz NC exhibiting the (100) and (101) planes and the angle between the (100) and (101) planes is 38.1°. (D) Fast Fourier transform image of Fig. 2C.

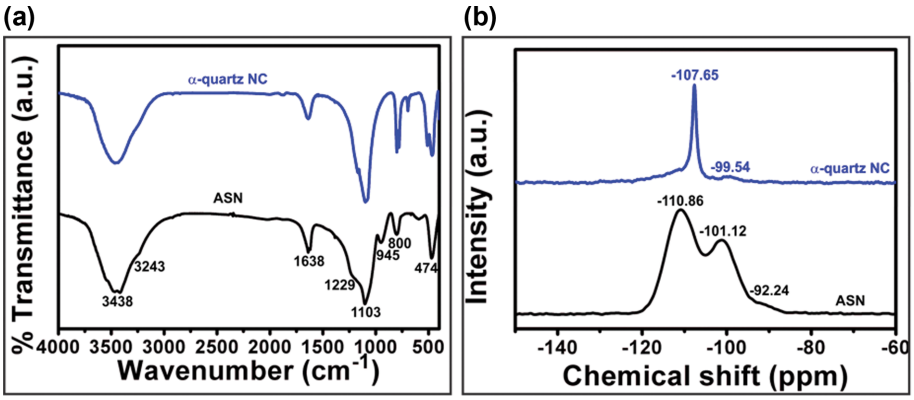

Fig. 3. (a) FT-IR and (b) ^{29}Si ssNMR spectra of α-quartz NCs (blue curve) and ASNs (black curve).

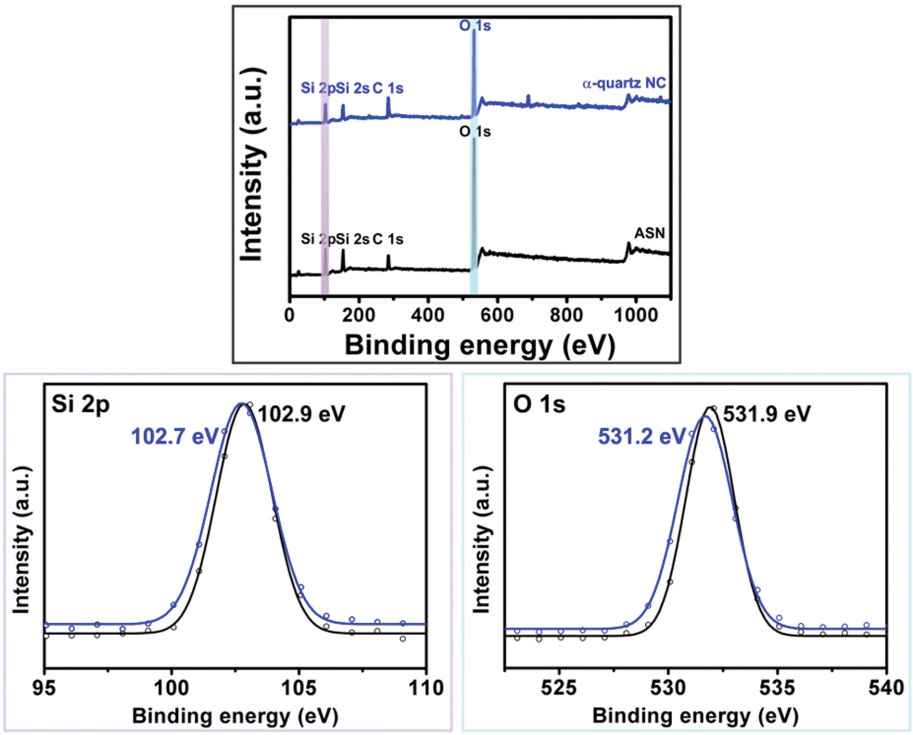

Fig. 4. (Top) Survey XPS spectra of α-quartz NCs (blue curve) and ASNs (black curve). (Bottom) High resolution XPS spectra of α-quartz NCs (blue curve) and ASNs (black curve). Open circles were obtained from XPS measurements, and solid curves were best fits obtained by Lorentzian-Gaussian deconvolution showing the binding energies (BEs) of the Si 2p (left) and O 1s (right).

ings calculated from its SAED pattern. Also, these assignments are in excellent agreement with the XRD results (Fig. 2A).

Fig. 3 presents FT-IR and ^{29}Si ssNMR measurements of the ASNs and as-synthesized NCs. The FT-IR spectra of the as-synthesized α-quartz NCs (blue curve, Fig. 3(a)) exhibit IR absorption bands at 3,438 and 3,243 cm^{-1}, which are assigned to the OH stretching vibration of adsorbed water and surface silanol [40]. The band at 1,638 cm^{-1} is assigned to bending vibration of adsorbed water [40]. The IR bands at 1,103, 800, and 474 cm^{-1} are assigned to asymmetric, symmetric stretching, and symmetric bending of Si-O-Si moieties. In general, the FT-IR spectrum obtained from α-quartz NCs is analogous to the spectrum from ASNs except for the fingerprint region from 1,000 to 400 cm^{-1} and a missing band at 945 cm^{-1}, which is due likely to fewer free hydroxyl groups bound to the surface Si atoms of α-quartz NCs [29,30]. ^{29}Si ssNMR spectrum of ASNs (black curve, Fig. 3(b)) shows three distinct peaks assigned to dihydroxy terminated Q^2 ($(-O)_2Si(OH)_2$) (δ=−101.12 ppm), monohydroxy terminated Q^3 ($(-O)_3Si(OH)$) (δ=−110.86 ppm), and nonhydroxy terminated Q^4 ($(-O)_4Si$) sites (δ=−92.24 ppm), respectively. In contrast, ^{29}Si ssNMR spectrum of α-quartz NCs (blue curve, Fig. 3(b)) shows only one major Q^4 peak (δ=−107.65 ppm) with a much narrower spectral width and one minor Q^3 shoulder peak (δ=−99.54 ppm), indicating the variation in Si-O-Si angles from that in the NCs with ordered silica networks smaller than those of ASNs with disordered networks [30].

Fig. 4 shows the survey XPS spectra of the ASN and NCs over

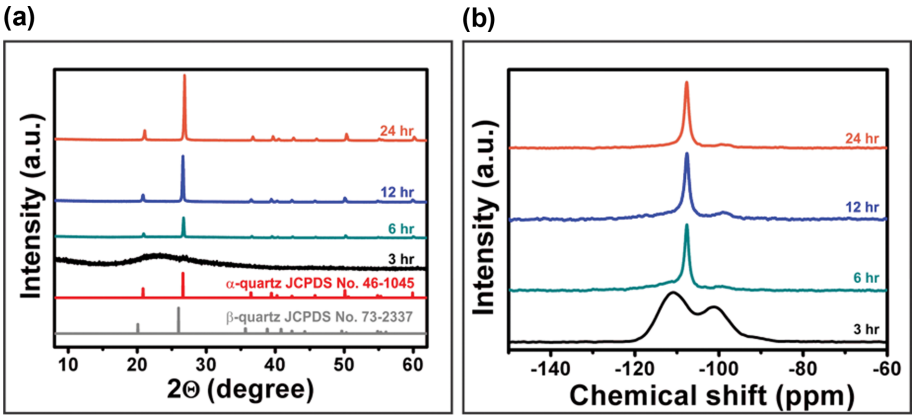

Fig. 5. Series of (a) XRD patterns and (b) ^{29}Si ssNMR spectra of the reaction products from ~3 (black curve), ~6 (dark cyan curve), ~12 (blue curve), and ~24 (orange curve) hr hydrothermal growth process.

the full energy range confirming the elements such as Si, O, and C. High resolution XPS spectra of ASNs and α-quartz NCs (black and blue circles, Fig. 4) were deconvoluted to obtain their best fits providing the following similar binding energies (BEs): Si 2p peaks at 102.9 and 102.7 eV and O 1s peaks at 531.9 and 531.2 eV, respectively. Given that BEs of 103.0 and 532.0 eV were used as reasonable reference values for the Si 2p and O 1s line in SiO_2 moieties, respectively [41], and that the Si 2p and O 1s spectra were best fitted with a single Gaussian peak, these peaks most likely originated from Si-O-Si environments with fewer Si-OH moieties [42].

A series of XRD was used along with ^{29}Si ssNMR measurements to monitor the growth process of the quartz NCs *ex-situ*. Fig. 5 shows that the products formed from a <~6 hr hydrothermal growth had only one and two broad peaks in the XRD pattern and ^{29}Si ssNMR spectrum, respectively (black curves, Fig. 5(a) and (b)). The spectral broadness of the XRD pattern and ^{29}Si ssNMR spectrum and the resemblance of ^{29}Si ssNMR spectrum to that of ASNs indicated that the products were likely amorphous. FESEM images of the products formed from 1-4 hr hydrothermal growth revealed that, initially, they were aggregated amorphous nanoparticles with an average size of ~37 nm (Fig. S5A). However, they appeared to form clusters of nearly uniform sizes that increased from ~60 nm (Fig. S5B) to ~196 nm (Fig. S5D) over the time period of ~2-4 hr. As the reaction time elapsed ~6 hr, two distinct changes occurred over the time period of 6-24 hr. First, the XRD patterns exhibited multiple peaks of which the intensity and the spectral width became more intense and narrower (dark cyan, blue, and orange curves, Fig. 5(a)), implying that increasing crystalline domain size greater than ~100 nm decreases XRD peak broadening [43] significantly. In fact, all the peaks in the XRD patterns were in good agreement with that of bulk crystalline α-quartz. Second, the ^{29}Si ssNMR spectra exhibited one major Q^4 and one minor shoulder Q^3 peak that was shifted slightly towards a less negative chemical shift. Their ssNMR spectral widths became much narrower (dark cyan, blue, and orange curves, Fig. 5(b)). These results suggest that the structure and crystalline order of the silica network likely began to emerge with less disparity in the Si-O-Si bond angles and more nonhydroxy terminated Q^4 sites during the NC growth process after an amorphous induction period [30].

N_2 sorption isotherms and thermogravimetric analysis (TGA) curves of the as-synthesized products (Figs. S3 and S4) showed their adsorption and weight loss characteristics. The shapes of all isotherms were similar to that of the characteristics type IV isotherms described in the IUPAC classification [44,45]. Notably, the isotherm shape of the aggregated amorphous nanoparticles formed from 3 hr hydrothermal growth exhibited the characteristic isotherm type H1 (IUPAC classification), which is commonly observed from nanostructured silica materials [46]. However, the isotherm shapes of the samples from 6-24 hr hydrothermal growth did not show distinctive hysteresis loop in their isotherms. Also, the specific surface areas of the samples formed at 3, 6, 12, 18, and 24 hr hydrothermal growth were determined to be 30.0, 7.7, 7.0, 7.8, and 5.3 $m^2 \cdot g^{-1}$ from their low temperature N_2 sorption isotherms using the BET model, respectively. The NCs exhibited significantly lower specific surface areas than the aggregated amorphous nanoparticles, likely due to their relatively larger sizes, higher crystallinity, and smoother crystal facet. TGA thermograph of the aggregated amorphous nanoparticles formed from 3 hr hydrothermal growth showed a maximum rate of weight loss (~4.5%) occurred in the region of 73-148 °C followed by another weight loss (~4.3%) around 223-512 °C, resulting in ~15% total weight loss over the entire temperature range. However, the NCs formed from 6-24 hr hydrothermal growth exhibited a gradual decrease in maximum rate of weight loss as the growth period is extended, resulting in only <~3% total weight loss. The decrease in weight loss is likely due to the crystalline state of the NCs, suggesting the thermal stability of the NCs is much superior to that of the amorphous nanoparticles.

The growth process was also examined by FESEM and TEM measurements on α-quartz NCs with sizes ranging from ~400 to ~800 nm. In particular, the length and width of the NCs measured along their long and short axes were plotted as a function of the reaction time t in Fig. 6. Length and width data measured only at 6-24 hr hydrothermal growth were considered for the NC growth stage and fitted by a power-law growth curve of the functional form At^{α}. A least-squares fit resulted in best fits with an exponent α of 0.50 and 0.52 and a pre-factor A of 171.20 and 102.33 for the length and width of the NCs, respectively. Surprisingly, the function was fitted well only with the data measured at 6-24 hr, as confirmed by

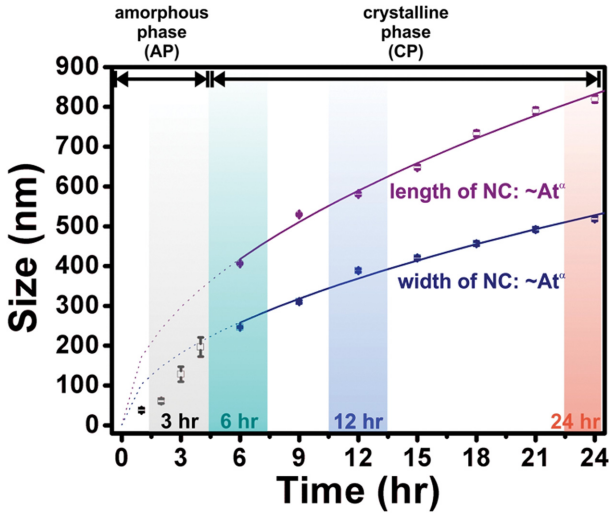

Fig. 6. Analysis of α-quartz NC growth kinetics showing the variation in length (purple curve) and width (dark blue curve) of the NCs measured at 6-24 hr after amorphous to crystalline transformation. The solid lines are best fits of the functional form At^{α} with an exponent α=0.50 and 0.52 and a pre-factor A of 171.20 and 102.23 (R^2=0.999 and 0.998) for the length and width of the NCs, respectively. The dotted lines are extrapolation to initial sizes at t=0. The black open squares correspond to the amorphous nanoparticle cluster sizes measured from FESEM images (Fig. S3) at ~1-4 hr and were not included in the fitting process.

$R^2 \approx 1$ (i.e., R^2=0.999 and 0.998 for the length and width of the NCs, respectively). These results suggest that the length of α-quartz NCs exhibited slightly faster growth along the *c*-axis than that of the width on the basal plane defined by the *a*-axis and *b*-axis. In the case of bulk quartz, the fastest growing face of bulk quartz under hydrothermal conditions was found to be the basal plane, and the order of rates was basal rate ((0001) equivalent to (001))>minor ((01$\bar{1}$1) equivalent to (011))>major rate ((10$\bar{1}$1) equivalent to (101))>>prism rate ((10$\bar{1}$0) equivalent to (100)) [32]. This is one of the reasons for the order of specific facet area to be prism ((100))> major ((101))>minor ((001)) shown in the model of anisotropic α-quartz crystal (inset image of Fig. 2B) [38,39]. The results of uneven growth rates indicate that there may be a tendency for quartz NC to exhibit an anisotropic morphology analogous to that of bulk quartz.

Fig. S5 shows FESEM images of the reaction products of aggregated nanoparticles and their clusters at ~1-4 hr. Analysis of nanoparticle cluster sizes vs. time showed that their sizes measured at ~1-4 hr (black squares, Fig. 6) were moderately comparable to the extrapolated values from the above power-law NC growth curve at ~3-6 hr. This result suggests that the sizes of amorphous silica formed from the dissolution of ASNs at amorphous phase (AP) may dictate the initial sizes of growing NCs at crystalline phase (CP) (Fig. 6). Thus the emergence of crystalline structure is not likely due to the sudden formation of NCs but rather to the amorphous to crystalline transformation of the clusters to NCs at ~3-6 hr.

The morphological and kinetic behavior of α-quartz NC growth can be understood by considering the classical principles to describe nanoparticle growth [47-62]. When nucleation occurs with constant monomer concentration during the growth of NCs, the cluster growth process begins to take place, which depletes the monomer concentration. Nucleation ceases when the concentration falls below a critical supersaturation and growth becomes the dominant process. Typically, a colloidal particle grows by the diffusion of monomers toward the surface, followed by a chemical reaction of monomers at the surface. In general, the surface-to-volume ratios of the smaller particles at the early growth stage are relatively high. Owing to the large surface areas, excess surface energy becomes more important in the smaller particles. The formation of large particles at the expense of small particles decreases the total surface free energy, which drives nanoparticle growth. This coarsening process in solution via atom-by-atom dissolution and reattachment, controlled either by mass transport or diffusion, is also known as an Ostwald ripening process [63]. The diffusion-limited Ostwald ripening process is the most predominant growth mechanism that was first quantified by Lifshitz and Slyozov [51], later reinforced by Wagner [59], and famously known as the Lifshitz-Slyozov-Wagner (LSW) theory. For a solid present at a solid-liquid interface, the chemical potential of a solid colloidal particle in solution environments increases with decreasing size. According to the Gibbs-Thompson equation [64], the equilibrium solute monomer concentration at the surface of larger particles is much lower than that of smaller ones. The resulting concentration gradients lead to the transport of the solute monomers from smaller particles to larger ones, which provides a driving force for the growth of larger particles at the cost of smaller particles. The coarsening process is often controlled by diffusion and particle growth via the addition of monomers to the particle surface from the solution.

In typical environments, the surrounding environment around NCs with an average radius of r, is considered to be the bulk liquid phase with a uniform supersaturated monomer concentration C_{sb}. In contrast, the monomer concentration at the interface between the liquid and the NC is C_i, and the solubility (i.e., equilibrium concentration) of the NC with a radius r is C_r. The net flux of monomers J moving through a spherical surface with radius x within the diffusion layer, which is known as Fick's first law of diffusion [65], is given by

$$J = 4\pi x^2 D\frac{dC}{dx} \tag{1}$$

where D is the diffusion coefficient of the monomer in the growth solution.

The situation where the flux is constant over the diffusion layer, of which its thickness is δ_r, is referred to as *steady-state*. Under the *steady-state*, the above differential equation can be integrated approximately using the intermediate value theorem, which is given by

$$J \cong \frac{4\pi Dr(r+\delta_r)}{\delta_r}(C_{sb} - C_i) \tag{2}$$

This flux can be equated to the consumption rate of the monomers at the NC surface, which is given by

$$J = 4\pi r^2 k_a (C_i - C_r) \tag{3}$$

where k_a is the rate constant of a first-order attachment reaction.

In many cases, it is difficult to measure or estimate C_i. Therefore, Eqs. (2) and (3) can be simplified by eliminating the variable C_i, which is given by

$$\begin{aligned} J\delta_r &= 4\pi Dr(r+\delta_r)(C_{sb}-C_i) \\ &= 4\pi Dr(r+\delta_r)\left(C_{sb}-\frac{1}{4\pi r^2 k_a}(J+C_r)\right) \end{aligned} \tag{4}$$

Simplifying Eq. (4) leads to

$$J=\frac{4\pi Dr\left(1+\frac{r}{\delta_r}\right)}{\left(1+\frac{D}{k_a r}\left(1+\frac{r}{\delta_r}\right)\right)}(C_{sb}-C_r) \tag{5}$$

Assuming the flux of monomers J passing through the infinitesimal thickness dr and time dt is approximately equal to

$$J\cong\frac{4\pi r^2 dr}{V_m dt} \tag{6}$$

where V_m is the molar volume of the particle. The rate of NC growth $\frac{dr}{dt}$ is expressed as

$$\frac{dr}{dt}=\frac{\frac{D}{r}\left(1+\frac{r}{\delta_r}\right)V_m}{\left(1+\frac{D}{k_a r}\left(1+\frac{r}{\delta_r}\right)\right)}(C_{sb}-C_r) \tag{7}$$

The dependence of C_{sb} and C_r on the NC size r due to the excess free energy of the surface is given by the Gibbs-Thompson relationship [64], which is expressed as follows:

$$C_r=C_e^{\infty}\exp\left(\frac{2\gamma V_m}{rRT}\right)\approx C_e^{\infty}\left(1+\frac{2\gamma V_m}{rRT}\right) \tag{8}$$

where C_e^{∞} is the equilibrium concentration of a bulk NC with an extremely flat geometry, γ is the interfacial energy, V_m is the molar volume of the particle, and R is the gas constant. When $\frac{2\gamma V_m}{rRT}$ is relatively very small, Eq. (8) can be simplified to retain only the first two terms of the Taylor expansion of the concentration. Similarly, C_{sb} can be approximated as

$$C_{sb}=C_e^{\infty}\exp\left(\frac{2\gamma V_m}{r_{sb}RT}\right)\approx C_e^{\infty}\left(1+\frac{2\gamma V_m}{r_{sb}RT}\right) \tag{9}$$

Because the thicknesses of the diffusion layers are typically on the order of micrometers and the radius of the NC is on the order of nanometers, it can be safely assumed that $r<<\delta_r$, which suggests that $1+\frac{r}{\delta_r}\approx 1$. Substituting Eqs. (8) and (9) into Eq. (7) with this assumption gives the rate of NC growth dr/dt, which is expressed as

$$\frac{dr}{dt}=\frac{2\gamma V_m^2 C_e^{\infty}}{\left(RT\left(\frac{1}{D}+\frac{1}{k_a r}\right)\right)}\left[\frac{1}{r}\left(\frac{1}{r_{sb}}-\frac{1}{r}\right)\right] \tag{10}$$

This study examined how the growth rate behaves at two different limits: diffusion-limited growth vs. reaction-limited growth. When diffusion is the slowest step in the growth process characterized by the condition, $D<<k_a r$ in Eq. (10), the diffusion of monomers to the surface of the NC essentially controls the growth. In this limit, Eq. (10) reduces to the following form:

$$\frac{dr}{dt}\cong\frac{2\gamma V_m^2 C_e^{\infty}}{\left(\frac{RT}{D}\right)}\left[\frac{1}{r^2}\left(\frac{r}{r_{sb}}-1\right)\right]=K_D\left[\frac{1}{r^2}\left(\left(\frac{r}{r_{sb}}\right)-1\right)\right] \tag{11}$$

where K_D is the proportionality constant given by $\frac{2\gamma D V_m^2 C_e^{\infty}}{RT}$. According to LSW theory, the ratio of the average radius to the critical radius at supersaturation $\left(\frac{r}{r_{sb}}\right)$ becomes constant, provided that the total mass of the system is conserved [51,59,62]. Applying this condition to Eq. (11) leads to the simplified form of the rate of growth expressed as follows:

$$\frac{dr}{dt}=K_D\left[\frac{1}{r^2}\left(\left(\frac{r}{r_{sb}}\right)-1\right)\right]\approx(\text{constant})\cdot K_D\frac{1}{r^2} \tag{12}$$

By solving the above simple differential equation, the dependence of the NC size on time r(t) is expressed as

$$r(t)^3-r(t=0)^3=K't,\ r(t)\propto t^{\frac{1}{3}} \tag{13}$$

where K′ is the proportionality constant, which is a function of the diffusion coefficient D and temperature T given by the expression,

$$K'=\frac{4}{9}K_D=\frac{8\gamma D V_m^2 C_e^{\infty}}{9RT} \tag{14}$$

where the diffusion coefficient of the system D is a function of temperature T as follows:

$$D=D_0\exp\left(-\frac{E_a}{k_B T}\right) \tag{15}$$

where k_B is the Boltzmann constant and E_a is the activation energy of the diffusing monomers.

In addition to the diffusion process that is well accounted for in the LSW theory, another crucial process in the growth of NC is the chemical reaction at the surface where the units of diffusing monomers are consumed into growing NCs by the attachment reaction. If the condition is at the opposite limit, i.e., $D>>k_a r$ in Eq. (10), the growth rate is instead limited by the surface chemical reaction of the monomers. Applying this condition to Eq. (10) leads to a simplification of the growth rate given by the following:

$$\begin{aligned} \frac{dr}{dt} &\cong\frac{2\gamma V_m^2 C_e^{\infty}}{\frac{RT}{k_a r}}\left[\frac{1}{r^2}\left(\frac{r}{r_{sb}}-1\right)\right] \\ &=\frac{2\gamma k_a V_m^2 C_e^{\infty}}{RT}\left[\frac{1}{r}\left(\left(\frac{r}{r_{sb}}\right)-1\right)\right] \\ &=K_R\left[\frac{1}{r}\left(\left(\frac{r}{r_{sb}}\right)-1\right)\right] \end{aligned} \tag{16}$$

where K_R is referred to as the kinetic coefficient that reflects the barriers to attachment and the geometric factors and is given by the expression

$$K_R=\frac{2\gamma k_a V_m^2 C_e^{\infty}}{RT} \tag{17}$$

The ratio $\left(\frac{r}{r_{sb}}\right)$ can be regarded as constant if the condition of mass conservation is met, similar to that of the diffusion-limited growth. Applying this condition to Eq. (16) leads to a simplification of the NC growth rate as follows:

$$\frac{dr}{dt} = K_R\left[\frac{1}{r}\left(\left(\frac{r}{r_{sb}}\right)-1\right)\right] \approx (\text{constant})\cdot K_R\frac{1}{r} \tag{18}$$

By solving this simple differential equation, the dependence of the NC size on time r(t) can be expressed as

$$r(t)^2 - r(t=0)^2 = K''t,\ r(t) \propto t^{\frac{1}{2}} \tag{19}$$

where K″ is the proportionality constant that is a function of the rate constant of a first-order attachment reaction k_a and temperature T.

Our results are in contrast with previous studies' results, including the growth of nanocrystalline agate and chalcedony quartz that yielded an exponent of ~1/6 with no physical meaning [34]. Considering that the dissolution of ASNs in aqueous solutions leading to the formation of (ortho)silicic acid (H_4SiO_4, SA),

$$SiO_2 + 2H_2O \rightarrow H_4SiO_4 \tag{20}$$

quartz crystals begin to grow by adding dissolved SA to their surfaces, edges, and corners layer by layer via a condensation reaction to form siloxane (Si-O-Si) bonds:

$$[Si_xO_y]-OH + H_4SiO_4 \rightarrow [Si_{x+1}O_{y+2}]-OH + 2H_2O \tag{21}$$

Given that exponents from the best fits to the data are close to 1/2 rather than 1/3 (Fig. 6), these results suggest that it is not diffusion-limited or dissolution-limited but reaction-limited over the flux of dissolved silicates as monomers, combined with the first-order kinetics of monomer attachment to the surface of the NC. While the exact form of the dissolved species was not determined, soluble silicate anions such as SiO_4^{4-} and $Si_3O_7^{2-}$ were likely formed in hydroxide rich alkaline environments [66].

Note that the characteristic diffusion length of the monomer is ~$(Dt)^{1/2}$, where t is the timescale of the system and D is the diffusivity of the monomer in solution. On the timescale of NC growth processes (5-24 hr), and for dissolved SA or silicic anion diffusivity of >~10^{-5} $cm^2 \cdot s^{-1}$ [67], the estimated diffusion length is ~100 μm. Because the characteristic diffusion length is much less than the distance to the autoclave walls, the concentration of monomers can be approximated as a constant across the NC surface by assuming the system as a semi-infinite volume. Furthermore, the characteristic diffusion length was much greater than the size of NCs, suggesting that the reaction at the NC surface may be much slower than the diffusion during the growth processes. Consequently, the condition $D \gg k_a r$ leading from Eq. (10) to Eq. (16) is justified. Furthermore, the anisotropic structure of quartz results in differences in growth rate in different crystallographic directions [24,25]. Differences between the attachment probabilities of dissolved silicate monomer and the surface energies γ in the direction of and perpendicular to the *c*-axis of α-quartz likely resulted in differences in the K_R, the K″, and the pre-factor A, which was likely responsible for different length and width growth rates. In conclusion, the overall square root of time dependence suggests that the α-quartz NC growth process is most likely driven by the enthalpic terms that give rise to the excess free energy. Moreover, the monomers combine into clusters, and the clusters grow into three dimensions. As the NC size increases, the NC growth rate slows, which is expected from the Gibbs-Thompson relationship.

Several studies have examined the growth kinetics of nanocrystals over the past decade [47,53,68-79]. In several cases, including Au [56,71,72,80-82], Ag [83,84], Pt [85], and ZnO [86,87] nanocrystals, there have been attempts to describe their growth processes in solutions using the LSW theory in the context of an Ostwald ripening mechanism. The dependence of their average size on time t during their growth processes has often been described using the general kinetic equation as follows:

$$\bar{d}^n(t) - \bar{d}^n(t_0) = K(t - t_0) \tag{22}$$

where $\bar{d}(t)$ and $\bar{d}(t_0)$ is the mean size of nanocrystals at time t and t_0. K is a temperature-dependent kinetic coefficient, and n is an exponent relevant to the coarsening mechanism. Plots of the mean size as a function of time t fit the parabola, indicating that the crystal size increases continuously with increasing time provided that the monomer feedstock is not insufficient. For example, the plots were almost linear with n≈3 for the case of Au nanocrystals, suggesting that the growth kinetics are controlled by the diffusion-limited Ostwald ripening process predicted by the LSW theory [80].

Although the growth models based on the Ostwald ripening mechanism have been applied widely, these findings cannot be explained and fitted adequately by diffusion-limited Ostwald ripening kinetics. Instead, these results are consistent with the model based on the reaction-limited growth kinetics because the growth kinetics exhibits the square root of time dependence. However, the square root of time dependence on the NC size alone is not enough to understand the overall mechanism of quartz NC growth. A few questions remain open concerning the analysis of the NC growth kinetics. First, these findings suggest the growth process likely involves an amorphous to crystalline transition at the early stages of NC growth. This transition typically took place at approximately 3-6 hr of reaction time. The time series of XRD patterns and ^{29}Si ssNMR spectra of the as-synthesized products (Fig. 5) confirmed the existence of the amorphous products. The similarity between the initial sizes of NCs and those nanoparticle cluster sizes corroborated the emergence of their crystallinity after the transformation. In short, our results exhibit the features of the amorphous to crystalline transformation, which the reaction-limited growth model cannot predict. Second, these results provide limited data of the measured sizes. This is because the measurements could not be performed *in-situ* due to the absence of a change in their size-dependent property that can be readily detected either by optical or scattering spectroscopy, particularly using synchrotron radiation with a sub-micron time resolution [88-90]. Although TEM is the most direct tool to analyze the size and size distribution of NCs, it is very time-consuming, making it almost impossible to follow the size and size distribution of a rapidly growing particle or NC during synthesis. While significant progress has been made to develop liquid-phase TEM for observing NC formation in real time [91], *in-*

situ monitoring of the growth of NCs in solution under hydrothermal conditions has not been demonstrated using liquid-phase due likely to the significant engineering challenges of maintaining higher temperatures and pressures within the TEM cells. On the other hand, monitoring of the growth of NCs in autoclave reactors at higher temperatures and pressures requires extra steps, such as cooling of the reactors followed by rapid sampling for TEM analysis. Unfortunately, this is a practical limitation of *ex-situ* experiments resulting in data acquisition with a relatively lower temporal resolution. Therefore, only the upper bounds of the induction period between the amorphous and crystalline transition were estimated to be ~3 hr. Third, the model assumes isotropic growth leading to a spherical morphology, which may not be most accurate at describing the system of quartz NCs exhibiting a high anisotropic morphology. Fourth, the growth data at the earlier growth stage ($0 \le t \le 6$ hr), although comparable to the initial sizes of NCs, were not rationalized by the model based on the reaction-limited control. One possible explanation is that the growth at the earlier stage may be driven either by an alternative mechanism, such as the aggregation or attachment of discrete amorphous particles, similarly known as a crystallographically controlled oriented attachment process [61,92], followed by amorphous to crystalline transition, or a combination of the Ostwald ripening and oriented attachment process. Further experimental and theoretical work will be needed to elucidate the mechanism of quartz NC growth at the earlier stages.

CONCLUSIONS

This paper presents a solution-phase synthesis to prepare highly uniform α-quartz NCs under mild hydrothermal conditions of ~250 °C and autogenic pressure. The structure, morphology, and composition of the NCs were characterized using the aforementioned analytical techniques. The as-synthesized NCs showed highly crystalline lattices of α-quartz with excellent thermal and chemical stability in acidic and basic aqueous environments. Their morphology shows a remarkable resemblance to bulk quartz crystal in its prism-like shape with six-sided pyramids at both ends. The hydrothermal growth of quartz NCs initially yielded the products of amorphous nanoparticles that were aggregated into clusters. The crystallinity of the products began to develop after the induction period. The comparable sizes of nanoparticle clusters to those of NCs and the emergence of crystallinity after the induction period indicate that the growth process likely involves an amorphous to crystalline transition. The length and width of NCs increased continuously with increasing time as NC growth proceeded. An analysis of the growth kinetics revealed a square root of time dependence that has not been observed from previous examples of growing quartz NCs. The simple model based on the square root of time dependence suggests that the growth process is reaction-limited, likely governed by controlling the dissolved silicate monomer flux to the surface of growing NCs followed by first-order rate-limiting attachment kinetics. Overall, the hydrothermal methods described offer a facile means of fine-tuning the sizes and morphologies of quartz NCs. Given their potential for advanced polishing and nanocomposite fabrication, high-quality and high-purity crystal growth, micro- and nano-electromechanical systems (MEMS and NEMS) devices based on nanoscale piezoelectricity, rechargeable battery devices, nanomaterial toxicology, and nanomaterial-based biorefinery applications, optimizing the synthesis of nanocrystals with desired properties is an important goal. Uncovering the complex nature of multi-step growth processes and understanding the growth kinetics is a significant step towards that goal.

ACKNOWLEDGEMENTS

This work was supported by the Financial Supporting Project of Long-term Overseas Dispatch of PNU's Tenure-track Faculty, 2020; Brain Korea 21 FOUR Program.

AUTHOR CONTRIBUTIONS

G.M. and S.C. designed research. G.M. and performed all experiments. S.C., G.M. and E.-H.J. analyzed data. S.C., G.M. and E.-H.J. prepared all figures. G.M., E.-H.J., S.K., Y.C., and S.C. wrote the paper.

DECLARATION OF CONFLICT OF INTEREST

The authors declare that there is no conflict of interest for the manuscript. The authors also declare that they have no known competing financial interests or personal relationships that could have influenced the work reported in the manuscript.

SUPPORTING INFORMATION

Additional information as noted in the text. This information is available via the Internet at http://www.springer.com/chemistry/journal/11814.

REFERENCES

1. H. Deng, J. Yin, J. Ma, J. Zhou, L. Zhang, L. Gao and T. Jiao, *Appl. Surf. Sci.*, **543**, 148821 (2021).
2. R. Geng, R. Chang, Q. Zou, G. Shen, T. Jiao and X. Yan, *Small*, **17**, 2008114 (2021).
3. C. Qian, J. Yin, J. Zhao, X. Li, S. Wang, Z. Bai and T. Jiao, *Colloids Surf. A Physicochem. Eng. Asp.*, **610**, 125752 (2021).
4. Y. Xu, R. Wang, J. Wang, J. Li, T. Jiao and Z. Liu, *Chem. Eng. J.*, **417**, 129233 (2021).
5. E. D. E. R. Hyde, A. Seyfaee, F. Neville and R. Moreno-Atanasio, *Ind. Eng. Chem. Res.*, **55**, 8891 (2016).
6. E. H. Jang, S. P. Pack, I. Kim and S. Chung, *Sci. Rep.*, **10**, 5558 (2020).
7. G. Qiao, L. Liu, X. Hao, J. Zheng, W. Liu, J. Gao, C. C. Zhang and Q. Wang, *Chem. Eng. J.*, **382**, 122907 (2020).
8. Z. Zhou, Y. Zheng, J. Gao, L. Jiang and Q. Wang, *J. Sol-Gel Sci. Technol.*, **77**, 205 (2016).
9. M. Pagliaro, *Silica-based materials for advanced chemical applications*, Royal Society of Chemistry (2009).
10. B. Mason and L. G. Berry, *Elements of mineralogy*, W. H. Freeman, San Francisco (1968).
11. K. I. Vatalis, G. Charalambides and N. P. Benetis, *Procedia Econ. Financ.*, **24**, 734 (2015).

12. A. Ballato, in *Piezoelectricity: Evolution and future of a technology*, W. Heywang, K. Lubitz and W. Wersing, Eds., Springer Berlin Heidelberg, Berlin, Heidelberg (2008).
13. Y. Saigusa, in *Advanced piezoelectric materials (second edition)*, K. Uchino, Ed., Woodhead Publishing (2017).
14. C. H. Yoder, in *Ionic compounds: Applications of chemistry to mineralogy*, Wiley (2006).
15. D. R. Spearing, I. Farnan and J. F. Stebbins, *Phys. Chem. Miner.*, **19**, 307 (1992).
16. P. Bettermann and F. Liebau, *Contrib. Mineral Petrol.*, **53**, 25 (1975).
17. W. S. Fyfe and D. S. McKay, *Am. Mineral.*, **47**, 83 (1962).
18. Y.-H. Jung, S. P. Pack and S. Chung, *Mater. Res. Bull.*, **101**, 67 (2018).
19. J. Liu, L. Wang, J. Wang and L. T. Zhang, *Mater. Res. Bull.*, **48**, 416 (2013).
20. X. Wang, J. Zhuang, Q. Peng and Y. D. Li, *Nature*, **437**, 121 (2005).
21. M. Yoshimura and K. Byrappa, *J. Mater. Sci.*, **43**, 2085 (2008).
22. K. Byrappa, N. Keerthiraj and S. M. Byrappa, in *Handbook of crystal growth*, P. Rudolph, Ed., Elsevier, Boston (2015).
23. O. Cambon and J. Haines, *Crystals*, **7**, 38 (2017).
24. P. R. Hervey and J. W. Foise, *Min. Metall. Explor.*, **18**, 1 (2001).
25. G. Johnson and J. Foise, in *Encyclopedia of applied physics*, G. L. Trigg, Ed., VCH Publishers (1996).
26. J. F. Bertone, J. Cizeron, R. K. Wahi, J. K. Bosworth and V. L. Colvin, *Nano Lett.*, **3**, 655 (2003).
27. P. Buckley, N. Hargreaves and S. Cooper, *Commun. Chem.*, **1**, 49 (2018).
28. X. M. Jiang, Y. B. Jiang and C. J. Brinker, *Chem. Commun.*, **47**, 7524 (2011).
29. G. Moon and S. Chung, *Appl. Chem. Eng.*, **31**, 697 (2020).
30. G. Moon, N. Lee, S. Kang, J. Park, Y.-E. Kim, S.-A. Lee, R. K. Chitumalla, J. Jang, Y. Choe, Y.-K. Oh and S. Chung, *Chem. Eng. J.*, **413**, 127467 (2021).
31. M. P. Finnegan, H. Zhang and J. F. Banfield, *Chem. Mater.*, **20**, 3443 (2008).
32. R. Laudise, *J. Am. Chem. Soc.*, **81**, 562 (1959).
33. K. Michibayashi and H. Imoto, *Phys. Chem. Miner.*, **39**, 213 (2012).
34. T. Moxon and M. Carpenter, *Mineral. Mag.*, **73**, 551 (2009).
35. W. J. de Ruijter, R. Sharma, M. R. McCartney and D. J. Smith, *Ultramicroscopy*, **57**, 409 (1995).
36. J. O. Malm and M. A. O'Keefe, *Ultramicroscopy*, **68**, 13 (1997).
37. P. D. Ihinger and S. I. Zink, *Nature*, **404**, 865 (2000).
38. G. S. Smith and L. E. Alexander, *Acta Crystallogr.*, **16**, 462 (1963).
39. P.-H. Wei, *Z Kristallogr*, **92**, 355 (1935).
40. M. Takeuchi, G. Martra, S. Coluccia and M. Anpo, *J. Near Infrared Specrosc.*, **17**, 373 (2009).
41. T. L. Barr, *Appl. Surf. Sci.*, **15**, 1 (1983).
42. P. Post, L. Wurlitzer, W. Maus-Friedrichs and A. P. Weber, *Nanomater.*, **8**, 530 (2018).
43. C. F. Holder and R. E. Schaak, *ACS Nano*, **13**, 7359 (2019).
44. P. B. Balbuena and K. E. Gubbins, *Langmuir*, **9**, 1801 (1993).
45. K. S. W. Sing, *Pure Appl. Chem.*, **57**, 603 (1985).
46. M. Thommes, K. Kaneko, A. V. Neimark, J. P. Olivier, F. Rodriguez-Reinoso, J. Rouquerol and K. S. W. Sing, *Pure Appl. Chem.*, **87**, 1051 (2015).
47. C. R. Bullen and P. Mulvaney, *Nano Lett.*, **4**, 2303 (2004).
48. V. LaMer, *Ind. Eng. Chem.*, **44**, 1270 (1952).
49. V. K. LaMer and R. H. Dinegar, *J. Am. Chem. Soc.*, **72**, 4847 (1950).
50. D.-K. Lee, S.-I. Park, J. K. Lee and N.-M. Hwang, *Acta Mater.*, **55**, 5281 (2007).
51. I. M. Lifshitz and V. V. Slyozov, *J. Phys. Chem. Solids*, **19**, 35 (1961).
52. X. Lin, C. Sorensen and K. Klabunde, *J. Nanopart. Res.*, **2**, 157 (2000).
53. X. Peng, J. Wickham and A. Alivisatos, *J. Am. Chem. Soc.*, **120**, 5343 (1998).
54. H. Reiss, *J. Chem. Phys.*, **19**, 482 (1951).
55. D. T. Robb and V. Privman, *Langmuir*, **24**, 26 (2008).
56. A. E. Saunders, M. B. Sigman and B. A. Korgel, *J. Phys. Chem. B*, **108**, 193 (2004).
57. T. Sugimoto, *Adv. Colloid Interface Sci.*, **28**, 65 (1987).
58. D. V. Talapin, A. L. Rogach, M. Haase and H. Weller, *J. Phys. Chem. B*, **105**, 12278 (2001).
59. C. Wagner, *Z. Elektrochem.*, **65**, 581 (1961).
60. J. Y. Rempel, M. G. Bawendi and K. F. Jensen, *J. Am. Chem. Soc.*, **131**, 4479 (2009).
61. F. Wang, V. N. Richards, S. P. Shields and W. E. Buhro, *Chem. Mater.*, **26**, 5 (2014).
62. R. Viswanatha and D. D. Sarma, in *Nanomaterials chemistry: Recent developments and new directions*, C. N. R. Rao, h.c. mult. A Müller, A. K. Cheetham Eds., Wiley-VCH Verlag GmbH & Co. KgaA (2007).
63. W. Ostwald, *Phys. Chem.*, **37**, 385 (1901).
64. M. Perez, *Scr. Mater.*, **52**, 709 (2005).
65. H. Tyrrell, *J. Chem. Educ.*, **41**, 397 (1964).
66. R. A. Laudise, *Chem. Eng. News*, **65**, 30 (1987).
67. L. Rebreanu, J.-P. Vanderborght and L. Chou, *Mar. Chem.*, **112**, 230 (2008).
68. Y. Chen, E. Johnson and X. Peng, *J. Am. Chem. Soc.*, **129**, 10937 (2007).
69. M. Drofenik, M. Kristl, A. Žnidaršič, D. Hanžel and D. Lisjak, *J. Am. Ceram. Soc.*, **90**, 2057 (2007).
70. N. R. Jana and X. Peng, *J. Am. Chem. Soc.*, **125**, 14280 (2003).
71. X. Ji, X. Song, J. Li, Y. Bai, W. Yang and X. Peng, *J. Am. Chem. Soc.*, **129**, 13939 (2007).
72. L. Meli and P. F. Green, *ACS Nano*, **2**, 1305 (2008).
73. M. P. Morales, T. González-Carreño and C. J. Serna, *J. Mater. Res.*, **7**, 2538 (1992).
74. C. B. Murray, D. J. Norris and M. G. Bawendi, *J. Am. Chem. Soc.*, **115**, 8706 (1993).
75. J. S. Owen, E. M. Chan, H. Liu and A. P. Alivisatos, *J. Am. Chem. Soc.*, **132**, 18206 (2010).
76. L. Qu, W. W. Yu and X. Peng, *Nano Lett*, **4**, 465 (2004).
77. S. Stoeva, K. J. Klabunde, C. M. Sorensen and I. Dragieva, *J. Am. Chem. Soc.*, **124**, 2305 (2002).
78. J. Thessing, J. Qian, H. Chen, N. Pradhan and X. Peng, *J. Am. Chem. Soc.*, **129**, 2736 (2007).
79. N. Zheng, J. Fan and G. D. Stucky, *J. Am. Chem. Soc.*, **128**, 6550 (2006).
80. R. Seshadri, G. N. Subbanna, V. Vijayakrishnan, G. U. Kulkarni, G. Ananthakrishna and C. N. R. Rao, *J. Phys. Chem.*, **99**, 5639 (1995).
81. S. L. Westcott, S. J. Oldenburg, T. R. Lee and N. J. Halas, *Langmuir*, **14**, 5396 (1998).
82. J. Y. Xiao and L. M. Qi, *Nanoscale*, **3**, 1383 (2011).
83. L. Lin, M. Chen, H. Qin and X. Peng, *J. Am. Chem. Soc.*, **140**,

17734 (2018).
84. R. Shankar, B. B. Wu and T. P. Bigioni, *J. Phys. Chem. C*, **114**, 15916 (2010).
85. A. Ruditskiy, M. Zhao, K. D. Gilroy, M. Vara and Y. Xia, *Chem. Mater.*, **28**, 8800 (2016).
86. E. M. Wong, J. E. Bonevich and P. C. Searson, *J. Phys. Chem. B*, **102**, 7770 (1998).
87. R. Viswanatha, S. Sapra, B. Satpati, P. V. Satyam, B. N. Dev and D. D. Sarma, *J. Mater. Chem.*, **14**, 661 (2004).
88. S. Cheong, J. Watt, B. Ingham, M. F. Toney and R. D. Tilley, *J. Am. Chem. Soc.*, **131**, 14590 (2009).
89. R. Viswanatha, H. Amenitsch and D. D. Sarma, *J. Am. Chem. Soc.*, **129**, 4470 (2007).
90. L. Y. Yao, Y. X. Zhu, C. Q. Liu, R. H. Jiao, Y. H. Lu and R. X. Tan, *J. Chromatogr. B: Anal. Technol. Biomed. Life Sci.*, **989**, 122 (2015).
91. T. J. Woehl, *Chem. Mater.*, **32**, 7569 (2020).
92. J. Zhang, F. Huang and Z. Lin, *Nanoscale*, **2**, 18 (2010).

Supporting Information

Hydrothermal synthesis and characterization of quartz nanocrystals - Implications from a simple kinetic growth model

Gyuseop Moon[‡], Eun-Hye Jang[‡], Seok Kim, Youngson Choe, and Sungwook Chung[†]

School of Chemical Engineering, Pusan National University, 2 Busandaehak-ro 63beon-gil, Geumjeong-gu, Busan 46241, Korea

(*Received 20 July 2021 • Revised 13 October 2021 • Accepted 24 October 2021*)

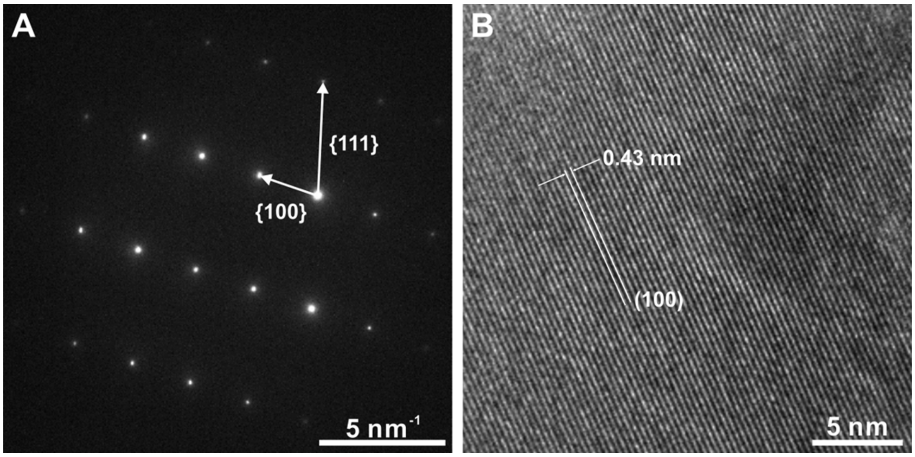

Fig. S1. (A) Selected area electron diffraction (SAED) pattern of α-quartz nanocrystal (NC). (B) Representative HRTEM image of α-quartz NC showing the lattice fringes spaced 0.43 nm that correspond to crystallographic (100) planes of α-quartz.

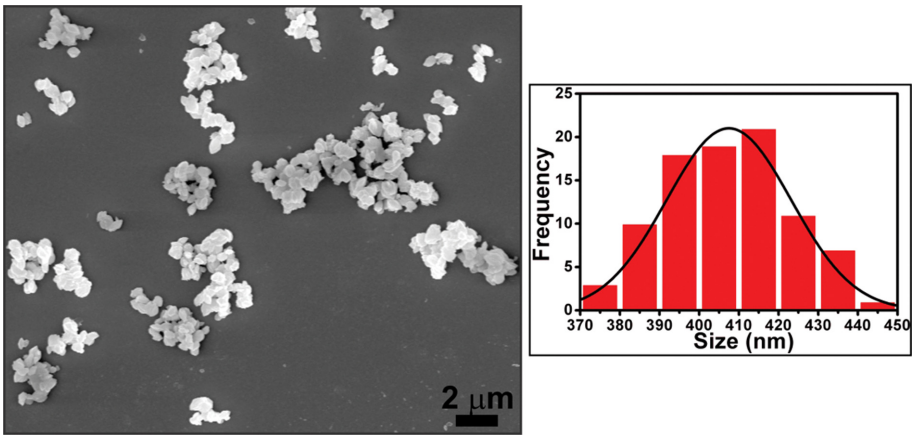

Fig. S2. Representative FESEM image of as-synthesized α-quartz NCs and their corresponding size distribution synthesized from ~6 hr reaction time (average size: 407±16 nm).

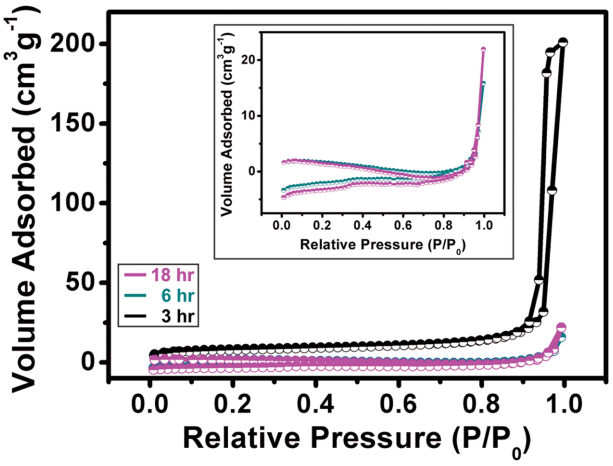

Fig. S3. N_2 sorption isotherm of the reaction products from ~3 (black curve), ~6 (dark cyan curve), and ~18 (pink curve) hr hydrothermal growth process.

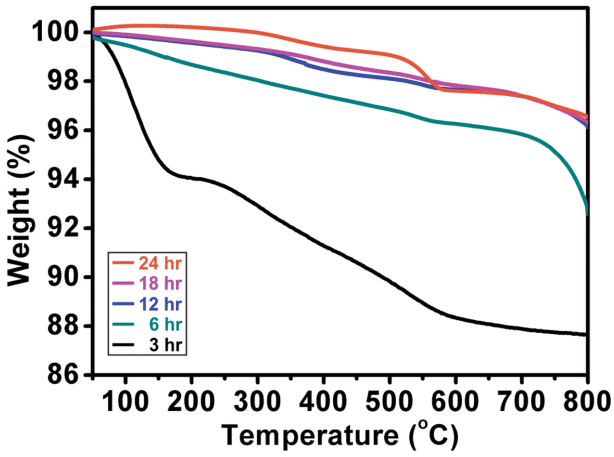

Fig. S4. TGA curves of the reaction products from ~3 (black curve), ~6 (dark cyan curve), ~12 (blue curve), ~18 (pink curve), and ~24 (orange curve) hr hydrothermal growth process showing their corresponding weight losses as a function of temperature.

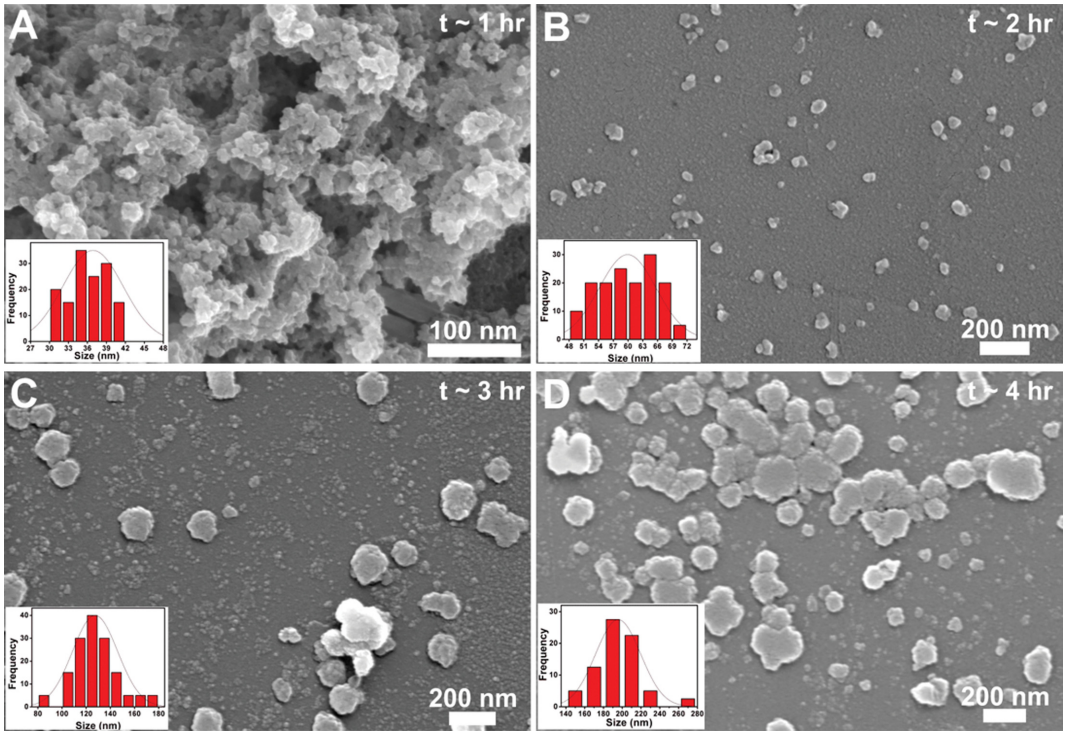

Fig. S5. FESEM images of the reaction products from (A) 1, (B) 2, (C) 3, and (D) 4 hr hydrothermal growth process. The inset histogram shows their corresponding size distribution with average size (A) 36.8±4.8, (B) 59.9±5.8, (C) 127.3±18.7, and (D) 195.6±24.0 nm.